ARTICLE

Joint PP- and PS-wave amplitude variation with angle inversion for thin interbeds

Peidong Huang[1], **Jun Lu[1]***, **Chun Yang[1]**, **Zhe Yang[2]**, and **Wei Yang[2]**

[1]Multi-Wave and Multi-Component Research Group, School of Geophysics and Information Technology, China University of Geosciences, Beijing, China

[2]Seismic Data Processing and Interpretation Center, Research Institute of Petroleum Exploration and Development-Northwest, PetroChina, Lanzhou, China

(This article belongs to the *Special Issue: Seismic Wave Propagation Theories and Reservoir Characterization Technologies for Complex Anisotropic Media*)

Abstract

Since transmission losses, internal multiples, and mode conversions are not considered, conventional inversion methods based on the Zoeppritz equations and related approximations have limited capability in high-resolution inversion of thin interbeds. Reflectivity methods, which account for these wave propagation effects, are more suitable for inverting thin interbeds; however, most related studies approximate thin interbeds as several isotropic thin beds, which are inadequate for complex thin interbeds containing thin vertical transverse isotropy (VTI) beds. In this study, thin VTI beds with the characteristics of short-term cycles are regarded as the fundamental compositional units of thin interbeds. We propose a joint PP- and PS-wave amplitude variation with angle inversion method for thin interbeds containing thin VTI beds. The method uses second-order approximations to the Kennett equations for thin interbeds containing thin VTI beds as the forward operator. The inversion objective function is established using the Levenberg–Marquardt algorithm, incorporating sparse constraints to improve the stability and resolution of the five-parameter inversion. Inversion results from model tests and field data demonstrate that the proposed method more accurately extracts elastic parameters and anisotropic information from thin interbeds compared to conventional methods based on the exact Zoeppritz equations, effectively improving inversion accuracy and offering a technical advancement for fine prestack inversion of complex thinly interbedded reservoirs.

Keywords: Amplitude variation with angle inversion; Reflectivity method; Sparse constraint; Thin interbeds; Vertical transverse isotropy

1. Introduction

As unconventional hydrocarbon exploration progresses, the study of wave propagation and parameter inversion in thin interbeds has received increasing attention, leading to greater demands for high-resolution exploration and parameterization of these thin interbeds. However, thin-interbed inversion faces two primary challenges. First, the thickness of thin beds within thin interbeds is generally smaller than the conventional

seismic resolution limit (usually <1/4 wavelength), making it difficult to accurately identify their internal structures. Second, the complex layered sedimentary structure causes significant transmission losses, internal multiples, and mode conversions in the wavefield of thin interbeds, complicating the accurate characterization of the wavefield and its propagation effects within the thin interbeds.

Conventional inversion methods for layered media are based on the exact Zoeppritz equations and their approximations, and researchers have made significant achievements in this field. Based on the Zoeppritz approximation, Buland and Omre[1] proposed a linear amplitude variation with offset (AVO) inversion method in a Bayesian framework and verified its accuracy through model testing. Huang et al.[2] introduced optimal transmission theory into the amplitude variation with angle (AVA) inversion of the exact Zoeppritz equations within a Bayesian framework. However, the Zoeppritz equations assume a single interface and do not account for transmission losses and internal multiples. This limitation impedes the accurate characterization of complex structures and wave propagation within thin interbeds, potentially leading to computational errors.[3]

The recursive matrix method offers more accurate calculations of transmission loss, internal multiples, and mode conversions than the Zoeppritz equations. This method has been widely applied to problems involving complex media and thin interbeds[4-8] and comprises the reflectivity method (RM) and the propagation matrix (PM). Kennett[9] provided the simplest recursive model of RM using a recursive algorithm, solving the overflow problem in the calculation of high-frequency and slowness exponential functions, ultimately making RM more suitable for research on thin interbeds. Rubino and Velis[10] proposed an AVA inversion method for thin beds based on acoustic wave theory and solved the highly non-linear constrained optimization problems associated with AVA inversion using simulated annealing. Padhi and Mallick[11] applied genetic algorithms to multi-component waveform inversion based on RM. In addition, Lu et al.[12] conducted an inversion of thin beds using the PM combined with the Levenberg–Marquardt (LM) algorithm to improve inversion accuracy. Yang and Lu[13] derived the Kennett's second-order approximations for thin interbeds based on Kennett's[9] recursive RM matrix. Yang and Wang[14] proposed a joint PP-PS prestack inversion method for thin beds based on the least-squares approach. The forward operator of this method was the PM, and its accuracy was verified using thin-bed model tests. Kuai et al.[15] developed a prestack inversion method based on the RM and LM algorithms to support the detailed identification of thin beds. Overall, these studies indicate that when inverting for thin beds and thin interbeds, both the RM and PM methods can produce detailed inversion results, enabling improved parameterization of internal characteristics.

Compared to conventional single-data processing and inversion, joint processing and inversion of PP and PS seismic data provide detailed parameter information.[16,17] Furthermore, incorporating multi-component data enables joint constraints and cross-validation during inversion, improving both resolution and stability. Veire and Landrø[18] proposed a joint inversion method for PP and PS seismic data that estimates the linear expressions of PP and PS reflection coefficients using least squares, enhancing the robustness of parameter estimation. Lu et al.[19] developed a stepwise anisotropic AVO inversion method for joint PP and PS seismic data based on the Rüger approximation[20] and genetic algorithms. Luo et al.[21] proposed a joint inversion method for PP and PS waves using the PM, optimizing the algorithm to improve the inversion speed and provide better parameter estimates compared to single-data inversions. Tura et al.[22] implemented joint inversion using PP and PS seismic data with both the model's inversion results and field data, indicating that joint inversion can more effectively identify the rock and fluid characteristics of the reservoir. Yang et al.[23] proposed a quadratic-reflectivity-based joint PP- and PS-wave inversion for vertical transverse isotropy (VTI) media, confirming its accuracy in predicting anisotropy through model testing. These studies demonstrate that joint inversion of PP and PS seismic data achieves higher accuracy and stability compared to single-data inversions. Given the complexity of thin interbed structures, we hypothesize that it is essential to introduce multi-component data into the inversion of thin interbeds.

Most existing studies consider thin interbeds as multilayer isotropic media, which tends to be accurate for simple thin interbeds. However, some complex thin interbeds contain thin beds with short-term cycle characteristics, where internal grain size shows rhythmic, periodic variations, or consist of multiple ultra-thin sublayers. These thin beds are horizontally isotropic but vertically anisotropic and can be classified as thin VTI beds. Currently, no suitable inversion methods exist for thin interbeds containing thin VTI beds. Inversions based on the assumption of isotropic layered media or equivalent thick VTI layers cannot accurately describe their internal structures, leading to errors in reservoir predictions. In addition, few studies have addressed the joint inversion of PP and PS seismic data specifically for thin interbeds.

We propose a joint PP- and PS-wave AVA inversion method for thin interbeds containing thin VTI beds. Based

on the work of Huang *et al.*,[24] we introduced the Kennett's second-order approximations for thin interbeds containing thin VTI beds to establish the objective function. Due to the numerous inversion parameters associated with VTI media, we utilized the LM method[25,26] combined with a sparse constraint to ensure inversion stability. PP and PS AVA data were used in joint AVA inversion to reduce errors caused by multiple solutions. The inversion was conducted in the PP time domain, necessitating a time-domain conversion of the PS data. When processing field data, coupling among different wavefields and the lack of accurate subsurface physical parameters complicated the accurate conversion or separation of internal multiples. Based on small-to-medium incident angles and the thin-layer assumption, we achieved precise time–domain conversion of the first reflections using multi-horizon constraints in the target area, enabling approximate conversion of internal multiples from the PS time domain into the PP time domain. In addition, we appropriately reduced the weight of the PS data in the inversion to minimize the impact of internal multiple conversion errors on the inversion results. Model tests and field data inversion demonstrated that our method accurately characterized wave propagation in thin interbeds containing thin VTI beds, yielding reliable inversion results.

2. Theory

2.1. Total reflection coefficients for thin interbeds containing thin VTI beds

The internal structure of thin interbeds is complex. Consequently, wave propagation effects within thin interbeds cannot be accurately described by the Zoeppritz equations or their approximations, which assume a single interface. Yang and Lu[13] derived second-order approximations of the Kennett equations for isotropic thin interbeds, neglecting high-order multiple terms that have minimal influence on the reflection coefficient calculations. Their study indicated that the approximations accurately computed the total reflection coefficient for each thin bed within the thin interbed, thereby enhancing computational efficiency. However, their approach assumes that every thin bed is isotropic. Under actual geological conditions, thin beds may exhibit consistent lithology but show vertical gradation in grain size due to complex geological processes, or they may consist of multiple ultra-thin sublayers of differing lithologies, both reflecting short-term cycle characteristics (Figure 1). In both cases, the characteristics of the thin beds deviate from those of the homogeneous medium, exhibiting VTI properties. When such thin VTI beds are irregularly interbedded with isotropic thin beds to form a thin interbed, the structure and wavefield propagation effects become highly complex. Therefore, the isotropic Kennett's second-order approximations are inadequate for accurately characterizing variations in reflection coefficients within such complex thin interbeds.

To address this limitation, Huang *et al.*[24] proposed second-order approximations of the Kennett equations suitable for thin interbeds containing thin VTI beds by replacing the original isotropic single-interface reflection coefficients with their VTI counterparts. The modified equation enables the calculation of total reflection coefficient matrices for both PP- and PS-waves in a thin VTI bed, accounting for all wave propagation types (PP, PS, SP, and SS) within the thin interbed. Kennett's recursive method[9] was then applied to compute the total reflection coefficient at any interface *n* within the thin-interbed
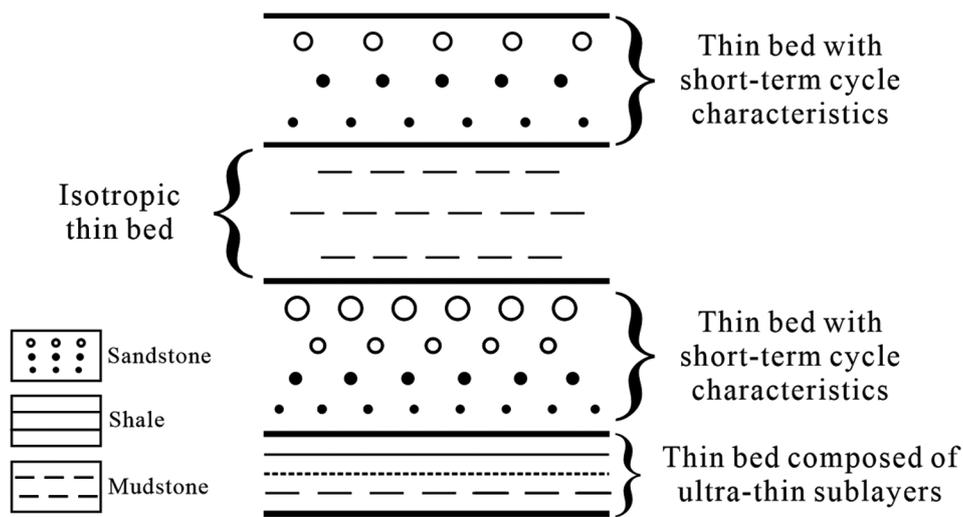

Figure 1. Sedimentary mode of a thin interbed containing thin vertical transverse isotropy beds

model (Figure 2) containing thin VTI beds in the slowness-frequency domain (**Equation 1**).

$$\check{\mathbf{R}}_{vD}^{(n)}\left(\mathbf{m},p,\omega\right)=\mathbf{R}_{vD}^{(n)}+\mathbf{T}_{vU}^{(n)}\mathbf{E}_{v}^{(n-1)}\mathbf{R}_{vD}^{(n-1)}\mathbf{E}_{v}^{(n-1)}$$
$$[\mathbf{I}+\mathbf{R}_{vU}^{(n)}\mathbf{E}_{v}^{(n-1)}\mathbf{R}_{vD}^{(n-1)}\mathbf{E}_{v}^{(n-1)}$$
$$+(\mathbf{R}_{vU}^{(n)}\mathbf{E}_{v}^{(n-1)}\mathbf{R}_{vD}^{(n-1)}\mathbf{E}_{v}^{(n-1)})^{2}]\mathbf{T}_{vD}^{(n)} \tag{1}$$

where **m** is the model parameter matrix, which is described in detail in Section 2.2, ω is the angular frequency, p is the horizontal slowness, and $\mathbf{R}_{vD}^{(n-1)}$, $\mathbf{R}_{vD}^{(n)}$, and $\mathbf{T}_{vD}^{(n)}$ are the reflection coefficient matrix of the downward wave interface $n-1$, the reflection coefficient matrix at interface n, and the transmission coefficient matrix of the downward wave at interface n, respectively. $\mathbf{R}_{vU}^{(n)}$ and $\mathbf{T}_{vU}^{(n)}$ are the reflection and transmission coefficient matrices of the upward wave at interface n, respectively. $\mathbf{E}_{v}^{(n-1)}$ is the phase-shift factor when the wave propagates from interface $n-1$ to n.

In **Equation 1**, $\mathbf{R}_{vD}^{(n)}$ is the primary reflection coefficient at interface n. $\mathbf{T}_{vU}^{(n)}\mathbf{E}_{v}^{(n-1)}\mathbf{R}_{vD}^{(n-1)}\mathbf{E}_{v}^{(n-1)}[\mathbf{I}+\mathbf{R}_{vU}^{(n)}\mathbf{E}_{v}^{(n-1)}\mathbf{R}_{vD}^{(n-1)}\mathbf{E}_{v}^{(n-1)}+(\mathbf{R}_{vU}^{(n)}\mathbf{E}_{v}^{(n-1)}\mathbf{R}_{vD}^{(n-1)}\mathbf{E}_{v}^{(n-1)})^{2}]\mathbf{T}_{vD}^{(n)}$ includes the primary reflection coefficient at interface $n-1$, along with the first- and second-order multiple reflection coefficients within layer $n-1$.

The total reflection coefficient matrix in **Equation 1** is expanded as **Equation 2**.

$$\hat{\mathbf{R}}_{vD}^{(n)}\left(\mathbf{m},p,\omega\right)=\begin{bmatrix}\hat{\mathbf{R}}_{PP} & \hat{\mathbf{R}}_{SP}\\ \hat{\mathbf{R}}_{PS} & \hat{\mathbf{R}}_{SS}\end{bmatrix}_{vD}^{(n)} \tag{2}$$

the terms $\hat{\mathbf{R}}_{PP}, \hat{\mathbf{R}}_{PS}, \hat{\mathbf{R}}_{SP}$, and $\hat{\mathbf{R}}_{SS}$ in **Equation 2** correspond to the total reflection coefficients of PP- and PS-waves for P-wave incidence, and of SP- and SS-waves for S-wave incidence, respectively. In the inversion, only the total reflection coefficients for the PP- and PS-waves are required. Therefore, **Equation 2** can be rewritten as **Equation 3**.

$$\hat{\mathbf{R}}_{vD}^{'(n)}\left(\mathbf{m},p,\omega\right)=\begin{bmatrix}\hat{\mathbf{R}}_{PP}\\ \hat{\mathbf{R}}_{PS}\end{bmatrix}_{vD}^{(n)} \tag{3}$$

Under the isotropic assumption, the single-interface coefficients in Kennett's second-order approximations are the displacement potential reflection and transmission coefficients. Huang et al.[24] replaced the isotropic single-interface reflection and transmission coefficients with those for VTI media, as proposed by Graebner.[27] Notably, the single-interface coefficients in Graebner's equations are the displacement reflection and transmission coefficients, which differ from those in the Kennett equations. Therefore, to convert Graebner's reflection and transmission coefficients into displacement potential coefficients, they must be multiplied by the corresponding velocity ratios, resulting in the displacement potential reflection and transmission coefficient matrices $\mathbf{R}_{vD}^{(n)}$, $\mathbf{T}_{vD}^{(n)}$, $\mathbf{R}_{vU}^{(n)}$, $\mathbf{T}_{vU}^{(n)}$, and $\mathbf{R}_{vD}^{(n-1)}$ (**Equation 4**).

$$\mathbf{R}_{vD}^{(n)}=\begin{bmatrix}\dfrac{V_{P}^{n}}{V_{P}^{n}}r_{PP} & \dfrac{V_{S}^{n}}{V_{P}^{n}}r_{SP}\\[2mm] \dfrac{V_{P}^{n}}{V_{S}^{n}}r_{PS} & \dfrac{V_{S}^{n}}{V_{S}^{n}}r_{SS}\end{bmatrix}_{D}^{(n)},\quad \mathbf{T}_{vD}^{(n)}=\begin{bmatrix}\dfrac{V_{P}^{n}}{V_{P}^{n-1}}t_{PP} & \dfrac{V_{S}^{n}}{V_{P}^{n-1}}t_{SP}\\[2mm] \dfrac{V_{P}^{n}}{V_{S}^{n-1}}t_{PS} & \dfrac{V_{S}^{n}}{V_{S}^{n-1}}t_{SS}\end{bmatrix}_{D}^{(n)},$$

$$\mathbf{R}_{vU}^{(n)}=\begin{bmatrix}\dfrac{V_{P}^{n-1}}{V_{P}^{n-1}}r_{PP} & \dfrac{V_{S}^{n-1}}{v_{P}^{n-1}}r_{SP}\\[2mm] \dfrac{V_{P}^{n-1}}{V_{S}^{n-1}}r_{PS} & \dfrac{V_{S}^{n-1}}{V_{S}^{n-1}}r_{SS}\end{bmatrix}_{U}^{(n)},\quad \mathbf{T}_{vU}^{(n)}=\begin{bmatrix}\dfrac{V_{P}^{n-1}}{V_{P}^{n}}t_{PP} & \dfrac{V_{S}^{n-1}}{V_{P}^{n}}t_{SP}\\[2mm] \dfrac{V_{P}^{n-1}}{V_{S}^{n}}t_{PS} & \dfrac{V_{S}^{n-1}}{V_{S}^{n}}t_{SS}\end{bmatrix}_{U}^{(n)},$$

$$\mathbf{R}_{vD}^{(n-1)}=\begin{bmatrix}\dfrac{V_{P}^{n-1}}{V_{P}^{n-1}}r_{PP} & \dfrac{V_{S}^{n-1}}{V_{P}^{n-1}}r_{SP}\\[2mm] \dfrac{V_{P}^{n-1}}{V_{S}^{n-1}}r_{PS} & \dfrac{V_{S}^{n-1}}{V_{S}^{n-1}}r_{SS}\end{bmatrix}_{D}^{(n-1)} \tag{4}$$
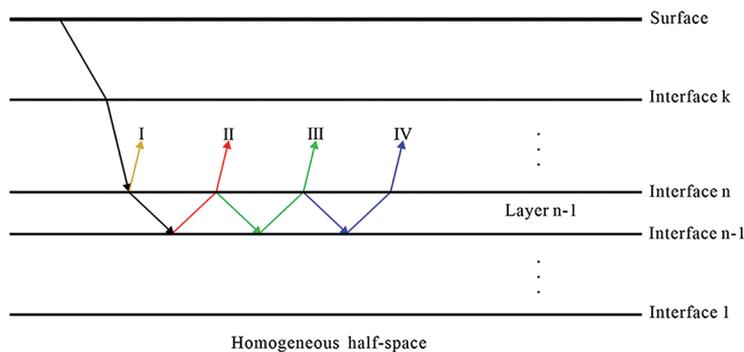

Figure 2. Wave propagation in a thin interbed model. I is the primary reflection at interface n, II is the primary reflection at interface $n-1$, III is the first-order multiple reflection of layer $n-1$, and IV is the second-order multiple reflection of layer $n-1$.

Where $r_{\ast\ast}$ and $t_{\ast\ast}$ in the matrices are the single-interface reflection and transmission coefficients, respectively, of the different modes proposed by Graebner. V_P and V_S represent the P- and S-wave velocities, respectively. The superscripts (n) and $(n-1)$ of the elements denote the corresponding layers of the medium.

The phase-shift factor in **Equation 1** ensures continuity of the phase when waves pass through an interface. The phase-shift factor matrix in the VTI medium is expanded as **Equation 5**.

$$\mathbf{E}_v^{(n-1)} = \begin{bmatrix} \exp(i\omega q_P^{(n-1)}(\theta_P)h^{(n-1)}) & \\ & \exp(i\omega q_S^{(n-1)}(\theta_S)h^{(n-1)}) \end{bmatrix} \quad (5)$$

where θ_P and θ_S are the incident angles of the P- and S-waves in the layer $n-1$, respectively; $q_P(\theta_P)$ and $q_S(\theta_S)$ are the vertical slowness values of the P- and S-waves, respectively; and $h^{(n-1)}$ is the thickness of the layer $n-1$. Since it is difficult to accurately determine the thicknesses of subsurface layers in field data, we discretize the parameter model in the time domain and treat each time sample as an individual interface. The thickness h between any two adjacent samples is calculated from the time sampling interval and the corresponding velocity (**Equations 6-8**).

For both $q_P(\theta_P)$ and $q_S(\theta_S)$:

$$q(\theta) = \frac{1}{\sqrt{2}}\sqrt{A_1 - \sqrt{A_1^2 - 4A_2}} \quad (6)$$

Where

$$A_1 = \frac{\rho}{c_{33}} + \frac{\rho}{c_{55}} - \left(\frac{c_{11}}{c_{33}} + \frac{c_{55}}{c_{33}} - \frac{(c_{13}+c_{55})^2}{c_{33}}\right)p^2(\theta),$$

$$A_2 = \left(\frac{c_{11}}{c_{33}}p^2(\theta) - \frac{\rho}{c_{33}}\right)\left(p^2(\theta) - \frac{\rho}{c_{55}}\right) \quad (7)$$

Where c_{11}, c_{33}, c_{55}, and c_{13} are the independent stiffness components[28]:

$$c_{33} = V_{P0}^2\rho,$$
$$c_{55} = V_{S0}^2\rho,$$
$$c_{11} = 2c_{33}\varepsilon + c_{33},$$
$$c_{13} = \sqrt{2c_{33}(c_{33}-c_{55})\delta + (c_{33}-c_{55})^2} - c_{55} \quad (8)$$

Where V_{P0}, V_{S0}, and ρ represent the vertical P-wave velocity, vertical S-wave velocity, and density, respectively. ε and δ are the Thomsen anisotropy parameters, with ε denoting the velocity difference between horizontal and vertical P-waves, and δ characterizing the coupling between near-vertical P- and SV-waves.

However, ε and δ are not always directly available from well logs or parameter models of field data. In such cases,

we derive the stiffness components using Backus averaging theory.[29] This theory provides an effective approximation for a finely layered medium. From the Backus averaging theory, a sequence of ultra-thin isotropic sublayers can be represented by an equivalent thin VTI bed whose stiffness components are derived from the elastic properties of each layer. For each ultra-thin isotropic sublayer, the Lamé parameters λ_i and μ_i can be calculated from well-log data as in **Equation 9**.

$$\lambda_i = \rho_i\left(V_{P,i}^2 - 2V_{S,i}^2\right),$$
$$\mu_i = \rho_i V_{S,i}^2 \quad (9)$$

Where $V_{p,i}$, $V_{s,i}$, and ρ_i are the P- and S-wave velocities and density at sample i of the well logs, respectively.

The equivalent stiffness components of the VTI medium are obtained by the Backus averaging (**Equation 10**):

$$\overline{C_{33}} = \left\langle\frac{1}{\lambda+2\mu}\right\rangle^{-1},$$

$$\overline{C_{55}} = \left\langle\frac{1}{\mu}\right\rangle^{-1},$$

$$\overline{C_{11}} = \langle\lambda+2\mu\rangle - 2\frac{\left\langle\frac{\lambda}{\lambda+2\mu}\right\rangle^2}{\left\langle\frac{1}{\lambda+2\mu}\right\rangle},$$

$$\overline{C_{13}} = \frac{\left\langle\frac{\lambda}{\lambda+2\mu}\right\rangle}{\left\langle\frac{1}{\lambda+2\mu}\right\rangle} \quad (10)$$

Where $\langle\circ\rangle$ denotes the thickness-weighted arithmetic average within a Backus window (**Equation 11**):

$$\langle f\rangle = \frac{\sum_i h_i f_i}{\sum_i h_i} \quad (11)$$

Where h_i is the thickness of the i-th layer (or the sampling interval) of the well log.

From the equivalent stiffness components, the Thomsen anisotropy parameters are computed as in **Equation 12**.

$$\varepsilon = \frac{\overline{C_{11}} - \overline{C_{33}}}{2\overline{C_{33}}},$$

$$\delta = \frac{\left(\overline{C_{13}} + \overline{C_{55}}\right)^2 - \left(\overline{C_{33}} - \overline{C_{55}}\right)^2}{2\overline{C_{33}}\left(\overline{C_{33}} - \overline{C_{55}}\right)} \quad (12)$$

For weakly anisotropic media, according to the Christoffel equation, the ray parameter for P-waves is given by **Equation 13**.

$$p_P(\theta_P) = \frac{\sin\theta_P}{V_{P0}\sqrt{1 + 2\varepsilon\sin^2\theta_P + 2\delta\sin^2\theta_P\cos^2\theta_P}} \quad (13)$$

and the ray parameter for S-waves is given by **Equation 14**.

$$p_S(\theta_S) = \frac{\sin\theta_S}{V_{S0}\sqrt{1 + 2\delta\sin^2\theta_S\cos^2\theta_S}} \quad (14)$$

The reflection coefficient matrix calculated from **Equation 2** is defined in the slowness-frequency domain, whereas the reflection coefficients used in the AVA inversion must be in the angle-time domain. Therefore, using the inverse Fourier transform and Snell's law, the total reflection coefficient in the angle-time domain can be obtained as in **Equation 15**.

$$\hat{R}_{vD}(m,\theta,t) = \frac{1}{2\pi}\int_{-\infty}^{\infty}\hat{R}_{vD}\left(m, p = \frac{\sin\theta}{V(\theta)}, \omega\right)e^{i\omega t}d\omega. \quad (15)$$

Matching the PS records to the PP time domain is essential because multi-wave joint inversion is performed. Therefore, the corresponding conversion factor for each sample when compressing the PS AVA gathers to the PP time domain is given by **Equation 16**.

$$\gamma_{ij} = 2\frac{V_{P,ij} + V_{S,ij}}{V_{P,ij}} \quad (16)$$

Where i and j represent the incidence angles and time samples, respectively.

2.2. Objective function and solution

Under the assumption of a VTI medium, the model parameter matrix is constructed as in **Equation 17**.

$$m = \begin{bmatrix} V_{P0} & V_{S0} & \rho & \varepsilon & \delta \end{bmatrix}^T \quad (17)$$

Where V_{P0}, V_{S0}, and ρ represent the parameter vectors of vertical P-wave velocity, vertical S-wave velocity, and density, respectively, and ε and δ denote the two Thomsen anisotropy parameter vectors.

The synthetic seismic record is expressed as in **Equation 18**.

$$d(m,\theta,t) = W(t)\hat{R}(m,\theta,t) \quad (18)$$

where θ is the incidence angle, t denotes the seismic travel time, and W is the wavelet matrix. $\hat{R}$ is the angle-time domain reflection coefficient matrix, which is calculated from the model parameter vector m.

The inversion objective function is established using the LM algorithm, incorporating a sparse constraint,[19] as shown in **Equation 19**.

$$J(m) = \left\|(H + \lambda_1 I)\Delta m - J^T d_{ref}\right\|^2 + \lambda_2\left\|\Delta m + m_{ref}\right\| \quad (19)$$

Where λ_1 is the damping factor, λ_2 represents the weight for the sparse constraint, J is the Jacobian matrix, H denotes the Hessian matrix $H = J^T J$, and I denotes the identity matrix. d_{ref} is the difference between the synthetic and observed seismic records (**Equation 20**).

$$d_{ref} = \begin{bmatrix} d_{PP} - s_{PP} \\ d_{PS} - s_{PS} \end{bmatrix} \quad (20)$$

Where d_{PP} and d_{PS} are the synthetic PP- and PS-wave seismic records, respectively, while s_{PP} and s_{PS} are in the corresponding observed seismic data.

The Jacobian matrix J in multi-wave joint inversion has the form shown in **Equation 21**.

$$J = \begin{bmatrix} \dfrac{\partial d_{PP}}{\partial m} \\ \dfrac{\partial d_{PS}}{\partial m} \end{bmatrix} = \begin{bmatrix} \dfrac{\partial d_{PP}}{\partial V_{P0}} & \dfrac{\partial d_{PP}}{\partial V_{S0}} & \dfrac{\partial d_{PP}}{\partial \rho} & \dfrac{\partial d_{PP}}{\partial \delta} & \dfrac{\partial d_{PP}}{\partial \varepsilon} \\ \dfrac{\partial d_{PS}}{\partial V_{P0}} & \dfrac{\partial d_{PS}}{\partial V_{S0}} & \dfrac{\partial d_{PS}}{\partial \rho} & \dfrac{\partial d_{PS}}{\partial \delta} & \dfrac{\partial d_{PS}}{\partial \varepsilon} \end{bmatrix} \quad (21)$$

Where m_{ref} is the difference between the initial model m_0 and the true model m_{true} (**Equation 22**):

$$m_{ref} = m_0 - m_{true}, \quad (22)$$

For field data, m_{true} is typically represented by well logs. When the objective function reaches a minimum, the estimated model parameters are optimally consistent with the observed data and prior information. Under this condition, where $J(m)$ approaches zero, we derive **Equation (23)**:

$$\begin{cases} \left\|(H + \lambda_1 I)\Delta m - J^T d_{ref}\right\|^2 \to 0 \\ \lambda_2(\Delta m + m_{ref}) \to 0 \end{cases} \quad (23)$$

Alternatively, under approximately ideal conditions, where the initial model is relatively close to the true model, the model parameter update matrix can be written as in **Equation 24**.

$$\begin{aligned} \Delta m &\cong \left[H + (\lambda_1 + \lambda_2)I\right]^{-1}\left[J^T d_{ref} + \lambda_2 m_{ref}\right] \\ &\cong \left[\begin{pmatrix} \dfrac{\partial d_{PP}}{\partial m} \\ \dfrac{\partial d_{PS}}{\partial m} \end{pmatrix}^T \begin{pmatrix} \dfrac{\partial d_{PP}}{\partial m} \\ \dfrac{\partial d_{PS}}{\partial m} \end{pmatrix} + (\lambda_1 + \lambda_2)I\right]^{-1} \\ &\quad \left[\begin{pmatrix} \dfrac{\partial d_{PP}}{\partial m} \\ \dfrac{\partial d_{PS}}{\partial m} \end{pmatrix}^T \begin{pmatrix} d_{PP} - s_{PP} \\ d_{PS} - s_{PS} \end{pmatrix} + \lambda_2 m_{ref}\right] \end{aligned} \quad (24)$$

Under this assumption, each iteration of $\Delta\mathbf{m}$ should be sufficiently small to ensure inversion stability.

3. Model test

3.1. Model test without noise

The parameters of the thin interbed model containing thin VTI beds used to test the inversion method are listed in Table 1.

The synthetic PP and PS AVA gathers, as shown in Figure 3, were generated using the RM based on second-order approximations of the Kennett equations. The frequency range was 0–105 Hz, and a 30 Hz Ricker wavelet was used as the source wavelet. Considering that the incident angle range for field data angle gathers is usually narrow, the angle range for this model was set to 5°–30° with an interval of 5°.

Inversions based on the Kennett's second-order approximations for thin interbeds containing thin VTI beds

Table 1. Model parameters

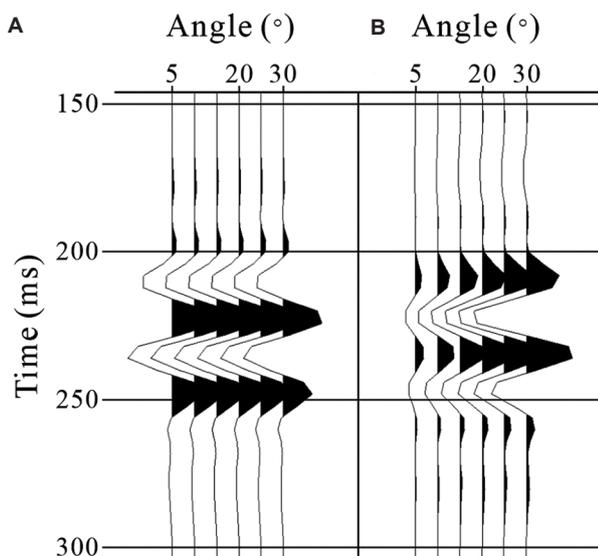| V_{P0} (km/s)	V_{S0} (km/s)	Density (g/cm³)	Thickness (m)	ε	δ
3.65	1.83	2.43	372	0.00	0.00
3.50	1.75	2.38	12	0.03	0.04
3.00	1.50	2.25	9	0.06	−0.03
3.50	1.75	2.38	12	0.03	0.04
3.00	1.50	2.25	9	0.06	−0.03
3.50	1.75	2.38	12	0.03	0.04
3.80	1.90	2.44	470	0.00	0.00

Figure 3. Synthetic amplitude variation with angle gathers of the thin interbed model described in Table 1. (A) PP (B) PS.

and the exact Zoeppritz equations were compared. Both methods used the same initial model and synthetic data. The inversion results obtained using the Kennett's second-order approximations for the thin interbeds containing thin VTI beds and the exact Zoeppritz equations are shown in Figures 4 and 5, respectively.

A quantitative comparison of the relative-error curves—defined as the absolute ratio of the difference between inverted and true values to the true value—for the five inverted parameters (V_{P0}, V_{S0}, ρ, ε, and δ) is shown in Figure 6. For V_{p0}, V_{s0}, and ρ, the relative error curves of the inversion results based on the Kennett's second-order approximations for thin interbeds containing thin VTI beds show smaller deviations and greater consistency with the true model. In contrast, the relative-error curves of the inversion results based on the exact Zoeppritz equations display larger fluctuations. Moreover, the inversion results based on the Kennett's second-order approximations maintain low relative errors for the Thomsen anisotropy parameters ε and δ, demonstrating the robustness of the proposed method for handling the complex wave propagation effects within thinly layered VTI media.

We also calculated the correlation coefficients between the inversion results obtained by the two methods and the true model. For the inversion based on the Kennett's second-order approximations for thin interbeds containing thin VTI beds, the correlation coefficients for V_{P0}, V_{S0}, ρ, ε, and δ are 0.995, 0.984, 0.989, 0.992, and 0.974, respectively; for the inversion based on the exact Zoeppritz equations, the coefficients for V_{P0}, V_{S0} and ρ are 0.978, 0.979, and 0.830, respectively. Inversion based on Kennett's second-order approximations achieves higher fit quality, with average coefficients of 0.987; in contrast, the fit quality of inversion based on the exact Zoeppritz equations yields lower values, with average coefficients of 0.932.

From a parameter-wise perspective, both Kennett's second-order approximations for thin interbeds containing thin VTI beds and the exact Zoeppritz equations provide high fits (>0.970) for V_{P0} and V_{S0}. For density ρ, the inversion based on Kennett's second-order approximations (0.989) significantly outperforms the inversion based on the exact Zoeppritz equations (0.830). By considering the VTI properties of thin VTI beds and the complex wave-propagation characteristics in thin interbeds, our method demonstrates a superior capability to resolve impedance-related parameters within thinly layered VTI media.

3.2. Model test with noise

To evaluate the robustness of the inversion method, 30% random noise was added to the PP and PS AVA gathers. The resulting synthetic records with noise are shown in
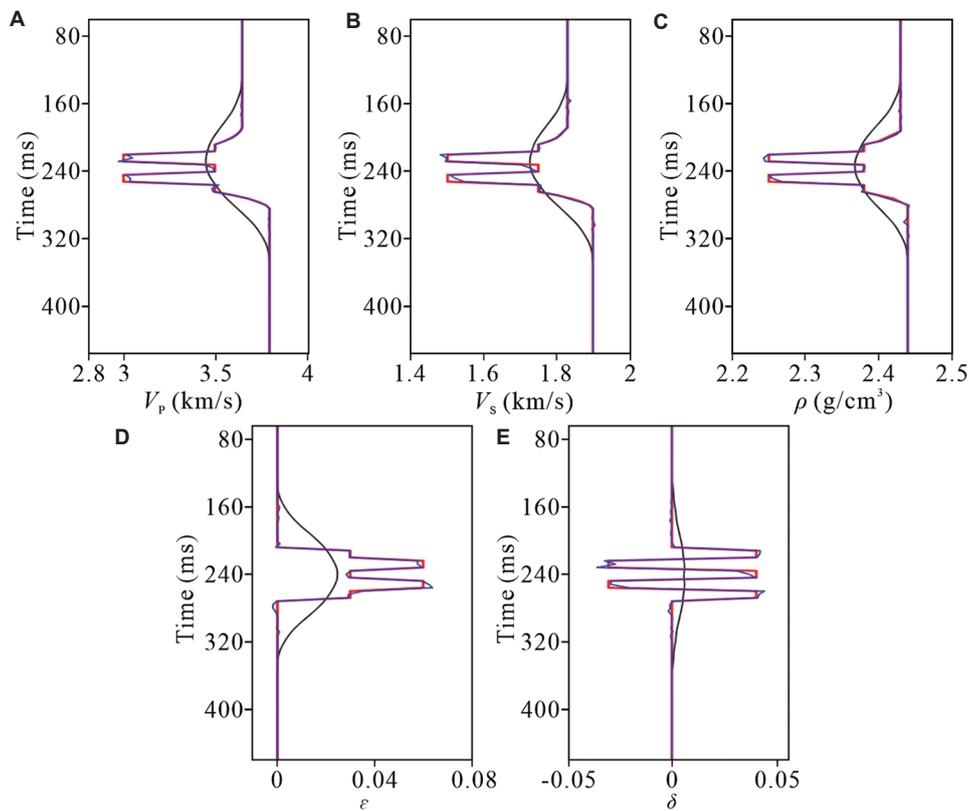
Figure 4. Inversion results of synthetic amplitude variation with angle gathers without noise, based on the Kennett's second-order approximations for thin interbeds containing thin vertical transverse isotropy beds. (A) P-wave velocity. (B) S-wave velocity. (C) Density. (D) ε. (E) δ. The black, red, and blue curves represent the initial model, true model, and inversion result, respectively.
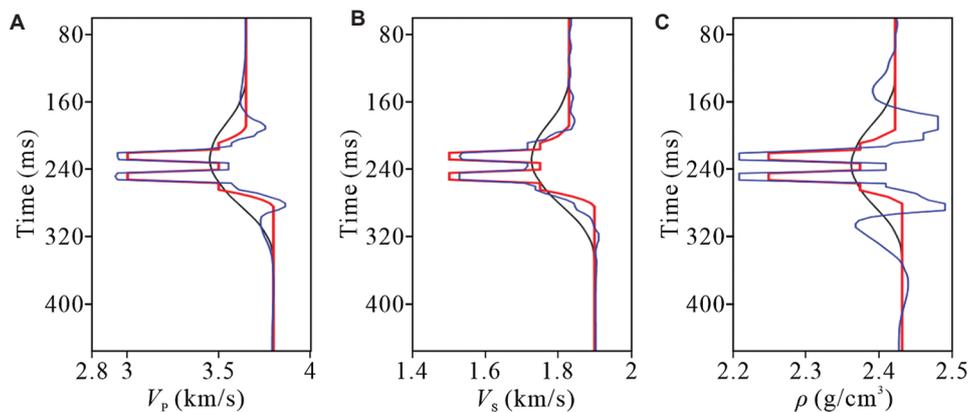

Figure 5. Inversion results of synthetic amplitude variation with angle gathers without noise, based on the exact Zoeppritz equations. (A) P-wave velocity. (B) S-wave velocity. (C) Density. The black, red, and blue curves represent the initial model, true model, and inversion result, respectively.

Figure 7. As shown in Figure 8, although the inversion results are noisy, they remain close to the true model, indicating that the inversion method has robust noise resistance.

4. Field data application

We applied our inversion method to multi-component surface seismic data from a mountainous oilfield. The shallow subsurface of this area features complex thin
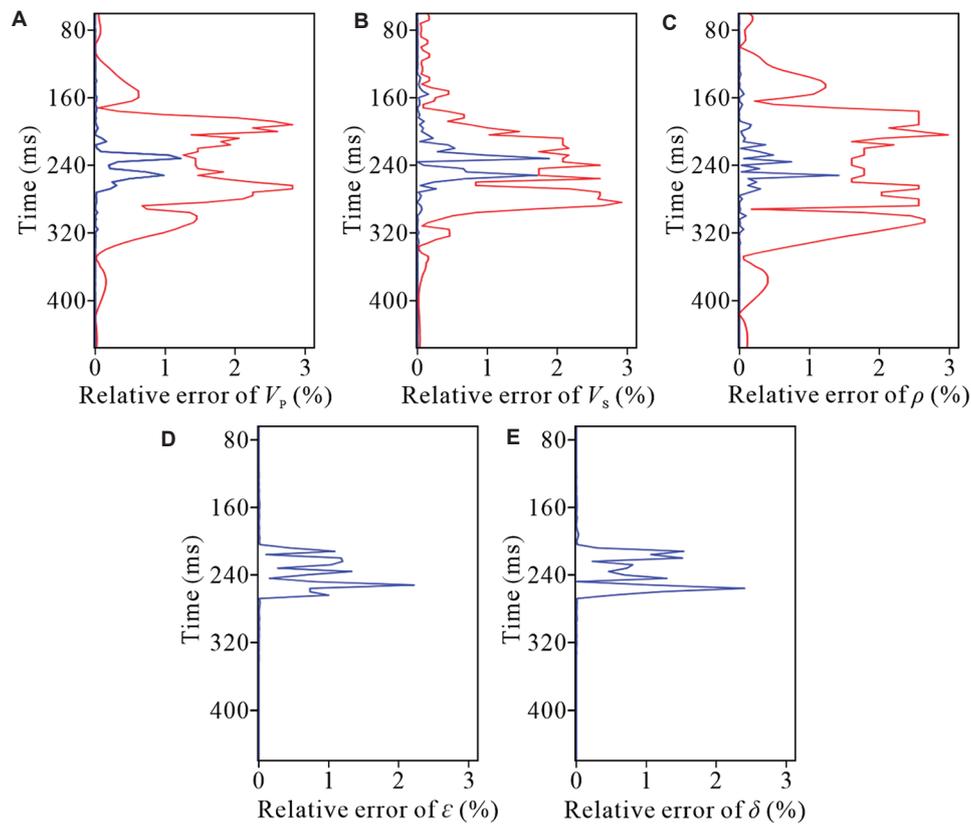
Figure 6. Relative-error curves between inversion results and the true model. (A) P-wave velocity. (B) S-wave velocity. (C) Density. (D) ε. (E) δ. The blue and red curves represent the relative-error curves of the inversion results based on Kennett's second-order approximations for thin interbeds containing thin vertical transverse isotropy beds and the exact Zoeppritz equations, respectively.
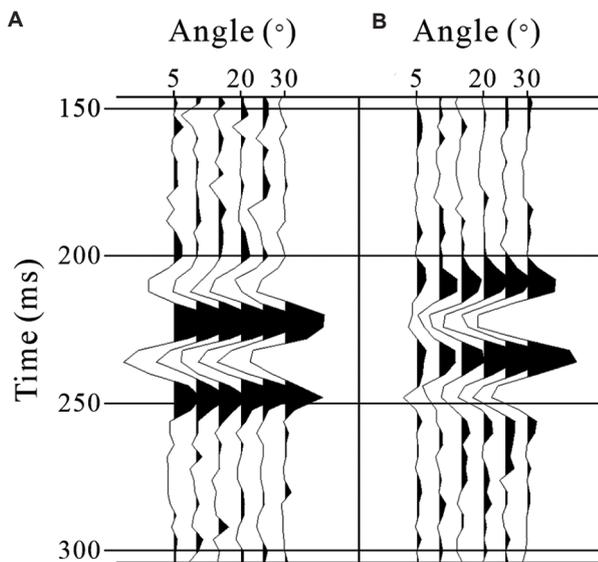

Figure 7. Synthetic amplitude variation with angle gathers of a thin interbed model described in Table 1 with 30% random noise. (A) PP. (B) PS.

interbeds of anisotropic sand and mudstone (shale). Due to limitations in the well logs, a 154–500 ms time interval was set as the inversion target. After Q-compensation, which estimated elastic wavefields, the PP and PS AVA gathers were generated from the field seismic data. These gathers were subsequently subjected to well-to-seismic calibration and multiple time-domain matching, resulting in AVA gathers in the PP time domain that were then matched with the well logs. The AVA gathers covered an angle range of 1°–15° at 2° intervals.

When compressing the PS AVA gathers from the PS time domain into the PP time domain, we observed that the travel times of the multiples differed from those of the primary reflections. Given that the primary target of our inversion method was thin interbeds, only internal multiples within them were considered. The travel time variations of internal multiples are complex and coupled with primary reflections, making it difficult to accurately compress the multiples in the PS AVA gathers into the
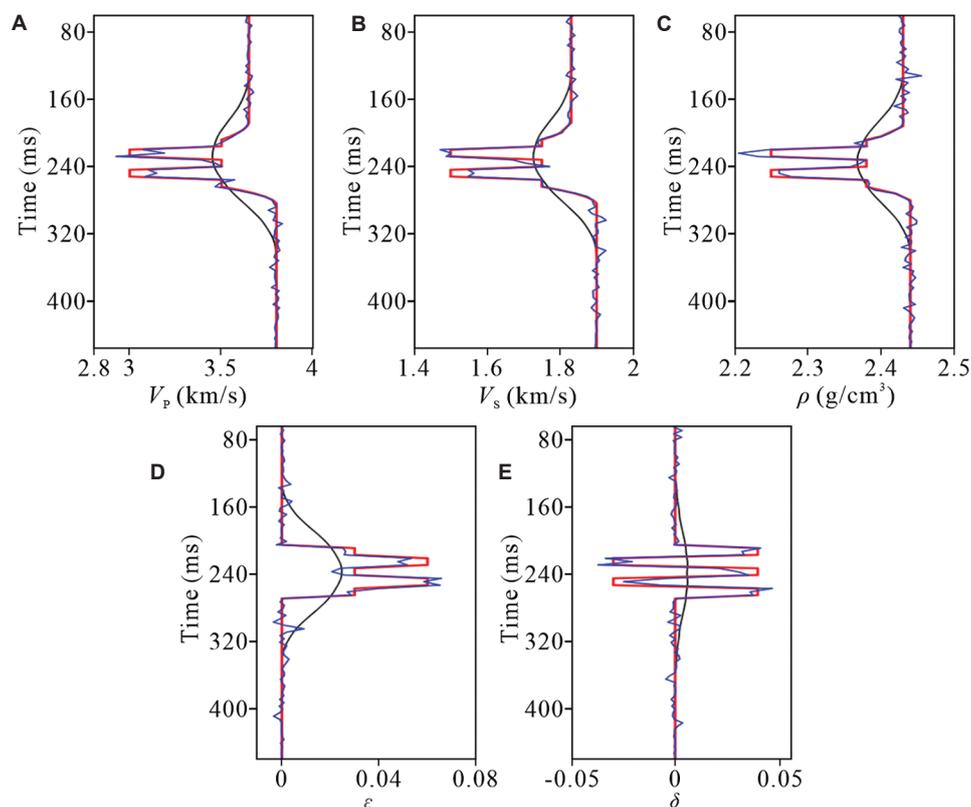
Figure 8. Inversion results of synthetic amplitude variation with angle gathers with 30% random noise, based on the Kennett's second-order approximations for thin interbeds containing thin vertical transverse isotropy beds. (A) P-wave velocity. (B) S-wave velocity. (C) Density. (D) ε. (E) δ. The black, red, and blue curves represent the initial model, true model, and inversion result, respectively.

PP time or to separate these multiples from the PS AVA gathers.

However, because of the small thickness of each thin bed, the time difference between the internal multiples and the primary reflections was minimal. Notably, our inversion method considered only first- and second-order multiples. In most cases, when the sampling rate is equal to or >2 ms, the time difference between the primary reflections and multiples is only approximately 2 to 3 sample points. Moreover, because the inversion was performed over small-to-medium incident angles, variations in the travel times of multiples with angle were negligible.

From these analyses, we constrained the time–domain conversion by including as many corresponding horizons as possible in the PP and PS AVA gathers, ensuring that the primary reflections of the PS AVA gathers were accurately converted into the corresponding PP times. This approach approximately converted the internal multiples within thin interbeds into their corresponding PP times. We then increased the weight of the PP AVA gathers in the inversion to minimize the impact of time errors in the PS AVA gathers on the inversion results.

Figure 9 shows the PP and PS wavelets extracted from the PP and PS AVA gathers in the PP time domain, with dominant frequencies of 20 Hz for both.

The P- and S-wave velocities and density were directly obtained from the measured well logs, whereas the anisotropic parameters ε and δ were estimated using Backus averaging theory based on **Equations 9-12**. These parameters were subsequently smoothed and served as the initial model for the inversion. Figure 10 shows the inversion results using the Kennett's second-order approximations for the thin interbeds containing thin VTI beds.

Since no other nearby well logs were available for cross-validation in the study area, the accuracy of the inversion results was evaluated by plotting the relative-error curves between the inversion results and the well logs. As illustrated in Figure 11, only a few samples exceeded 16% relative error, demonstrating that the inversion results achieve high accuracy even without incorporating the well logs as constraints in the initial model.

The correlation coefficients between the inversion results and the well logs for P- and S-wave velocities, density, ε, and δ were 0.720, 0.701, 0.867, 0.705, and 0.685,
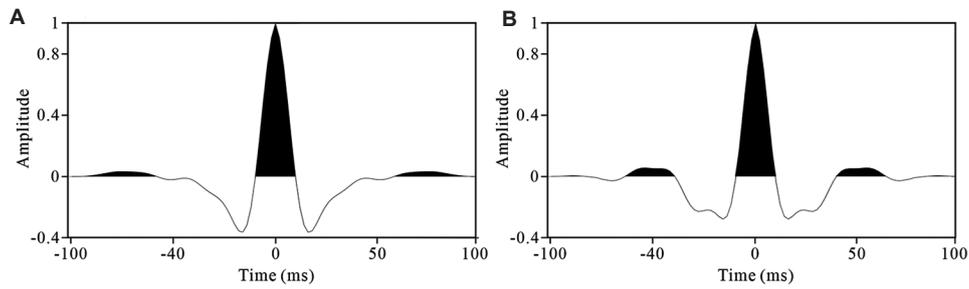
Figure 9. Wavelets extracted from the field data. (A) PP AVA gathers. (B) PS AVA gathers.
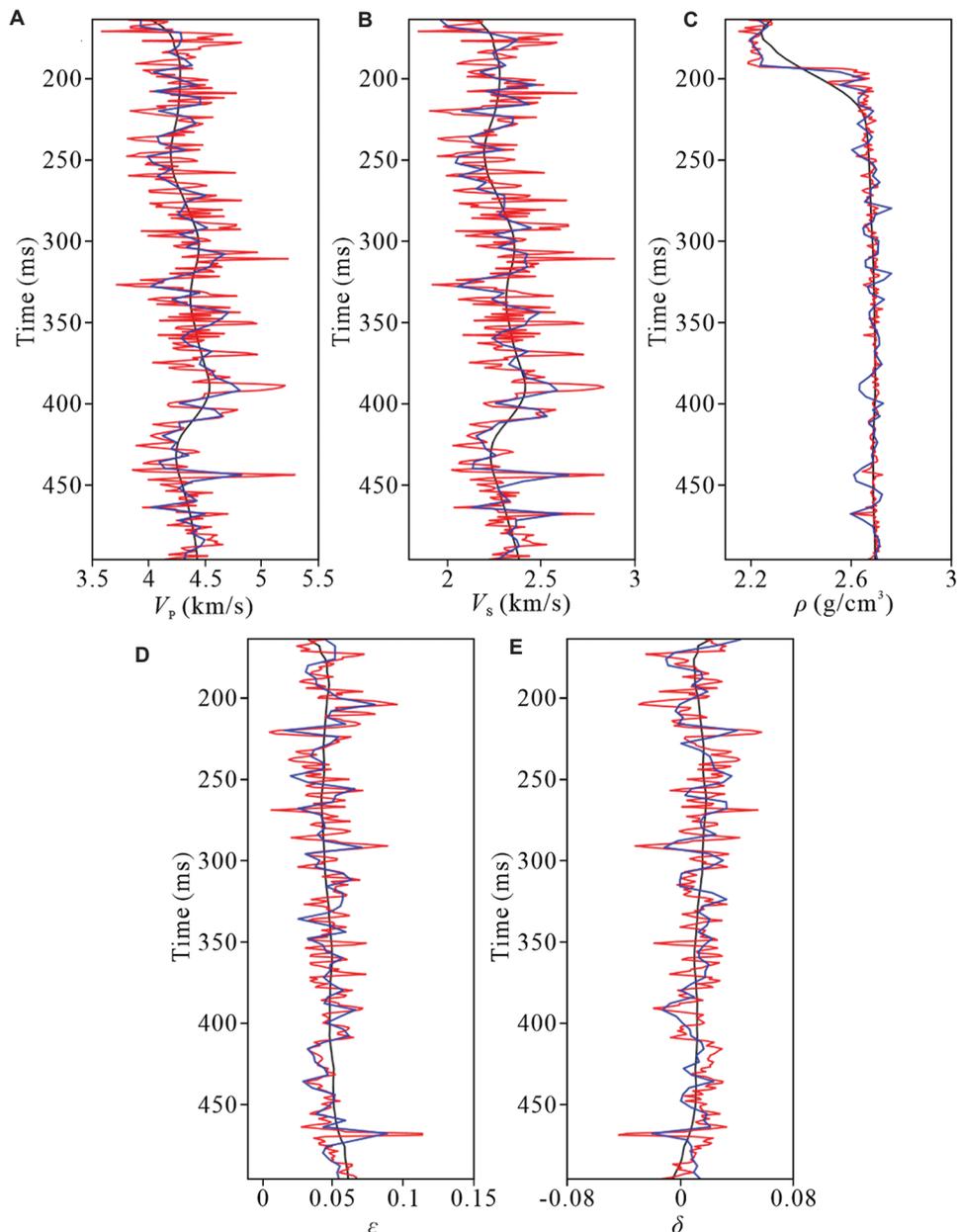Abbreviation: AVA: Amplitude variation with angle.

Figure 10. Inversion results of field data based on the Kennett's second-order approximations for thin interbeds containing thin vertical transverse isotropy beds. (A) P-wave velocity. (B) S-wave velocity. (C) Density. (D) ε. (E) δ. The black, red, and blue curves represent the initial model, well-log data, and inversion results, respectively.
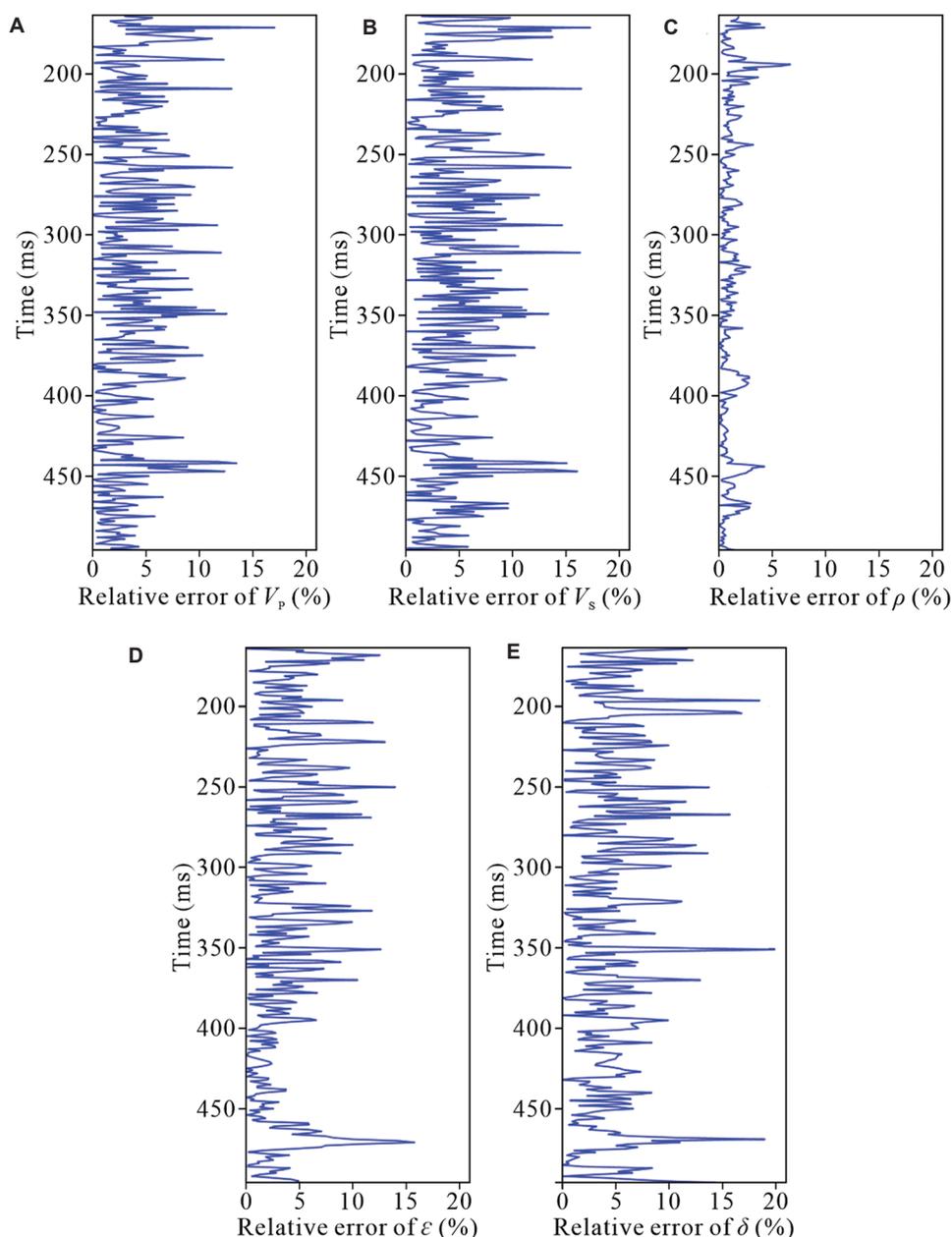
Figure 11. Relative-error curves between inversion results and the well logs. (A) P-wave velocity. (B) S-wave velocity. (C) Density. (D) ε. (E) δ.

respectively, indicating good consistency between the inversion results and the well logs. This error level indicates that the inversion method reliably captures the overall trends and key characteristics of the subsurface properties

Comparing the synthetic data with the field data (Figure 12) revealed that, despite the moderate quality of the field AVA gathers, our method still generated ideal synthetic AVA gathers. This observation indicates the robustness of the algorithm with the inclusion of the sparse constraint. The horizon and impedance relationships in

the synthetic AVA gathers were consistent with those in the surface seismic AVA gathers.

Based on the geological data, the one-dimensional initial models at the well location for P-wave velocity, S-wave velocity, density, ε, and δ were extended to create a two-dimensional initial model along the line (Figure 13), which was then used for the inversion.

The inversion results for the two-dimensional line are shown in Figure 14. Given the ability of the inversion method to characterize the physical parameters of thin

interbeds in detail, the inversion results can accurately describe the physical characteristics of a thin interbed containing thin VTI beds.

5. Discussion

The structural diversity within the thin interbeds leads to complex wavefield responses. Conventional methods
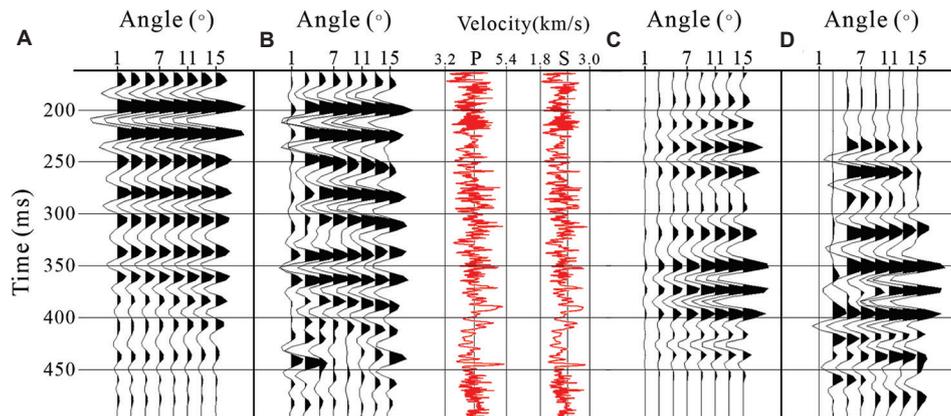

Figure 12. Comparison of synthetic and field AVA gathers. (A) Synthetic PP AVA gathers. (B) Field PP AVA gathers. (C) Synthetic PS AVA gathers. (D) Field PS AVA gathers. The red curves are the P- and S-wave velocities.
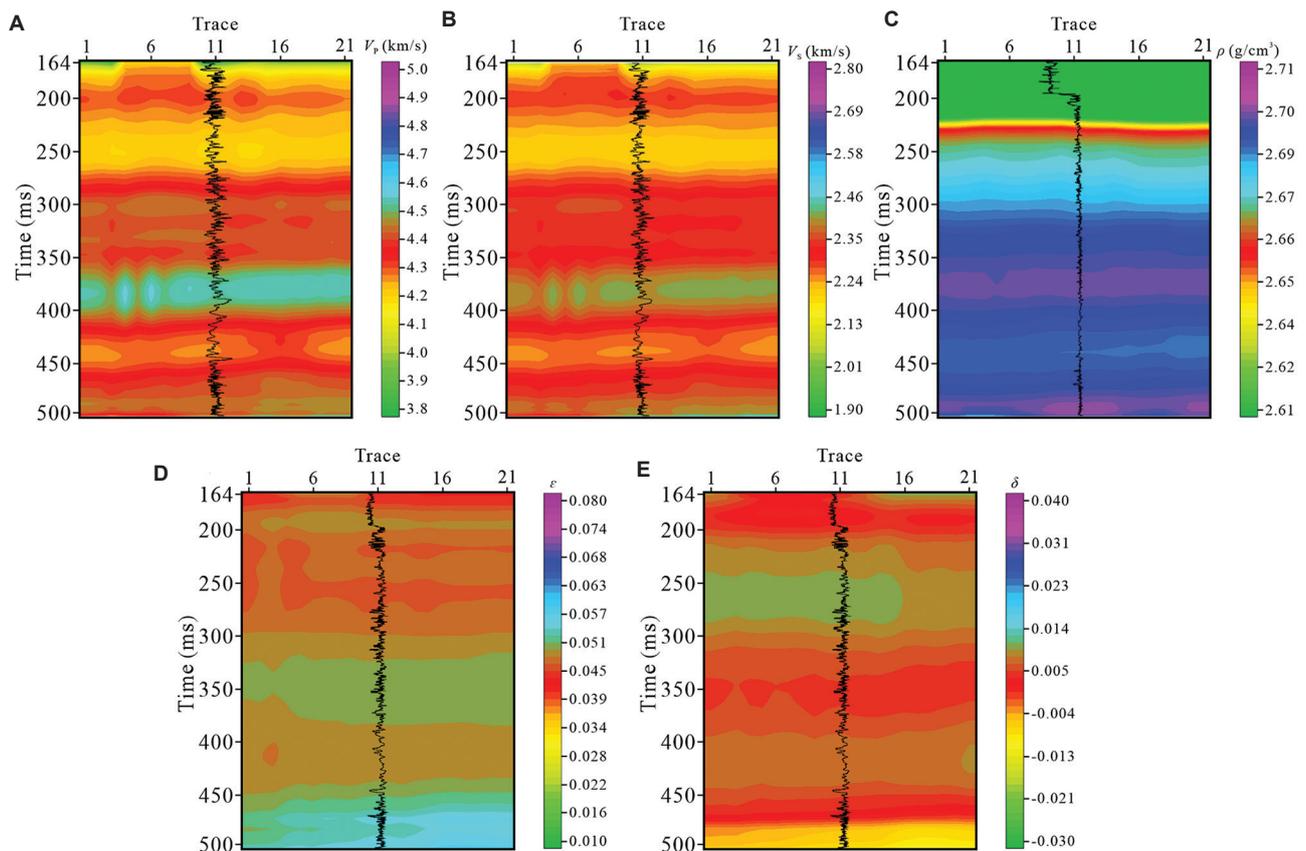Abbreviation: AVA: Amplitude variation with angle.

Figure 13. Two-dimensional initial model for inversion of field data. (A) P-wave velocity. (B) S-wave velocity. (C) Density. (D) ε. (E) δ. The black curves in (A), (B), and (C) are from the well logs corresponding to the parameter types, and the black curves in (D) and (E) are from gamma-ray log data.

Figure 14. Two-dimensional inversion results of field data. (A) P-wave velocity. (B) S-wave velocity. (C) Density. (D) ε. (E) δ. The black curves in (A), (B), and (C) are from the well logs corresponding to the parameter types, and the black curves in (D) and (E) are from gamma-ray log data.
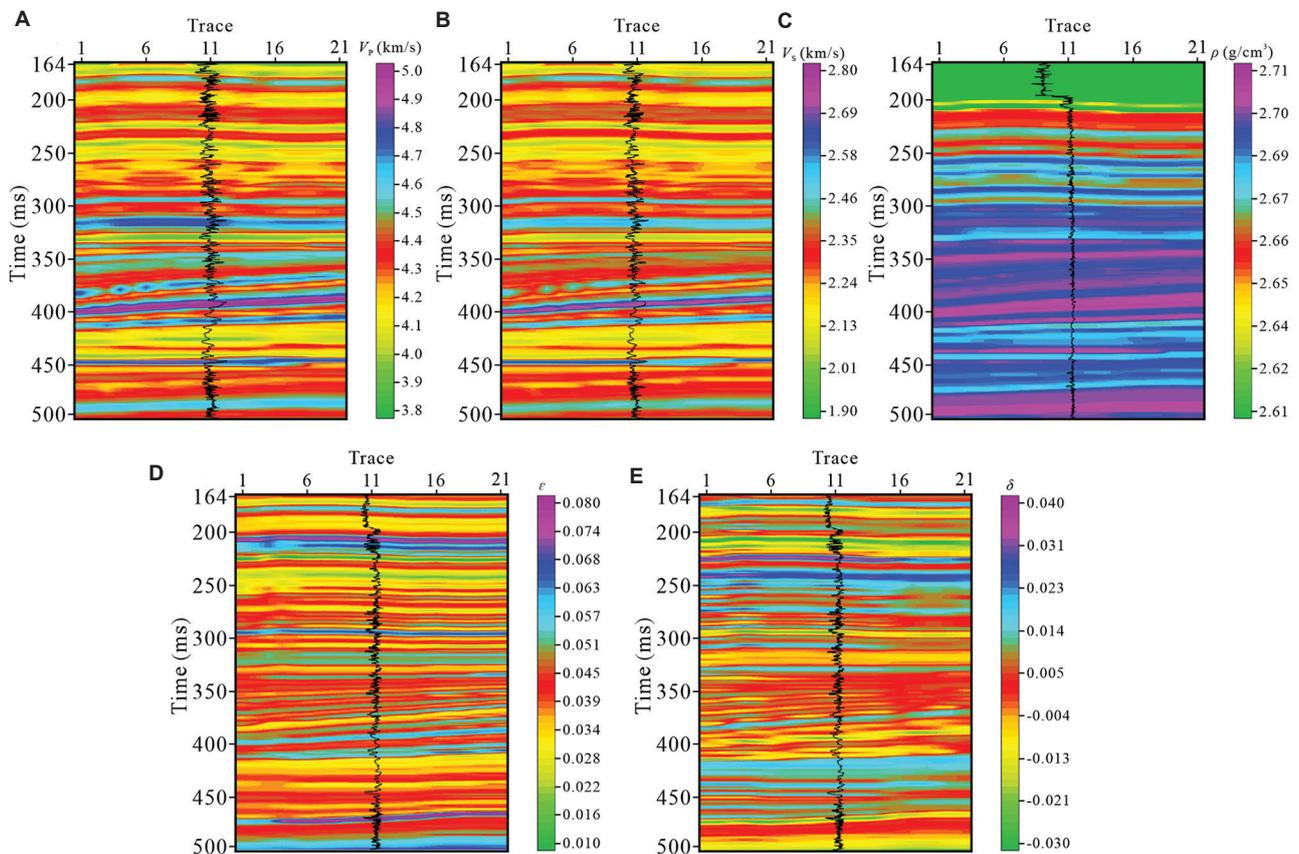
often treat thin interbeds as isotropic multilayer media or approximate them as thick VTI layers, extracting a single set of physical parameters from a thin interbed. Both approaches risk losing essential descriptions of the internal characteristics of thin interbeds.

In this study, we developed an inversion method for thin interbeds containing thin VTI beds, based on Kennett's second-order approximations. This method targets the geological features of thin beds with short-term cycle characteristics. By considering the VTI properties of thin beds within the interbeds, along with transmission losses, internal multiples, and mode conversions, the method effectively inverts velocity, density, and anisotropic parameter variation curves within the thin interbeds. The proposed inversion method is suitable for both thick and thin isotropic and VTI layers. In addition, the Kennett's second-order approximations accelerate the inversion by discarding higher-order terms that have minimal impact on the reflection coefficient calculations.

Compared to other least-squares methods, the LM algorithm is more stable when addressing complex anisotropic inversions. Based on this algorithm, we established an inversion objective function. Given that five parameters were inverted simultaneously, we incorporated a sparse constraint term into the objective function to limit model complexity, prevent overfitting, and reduce noise.

Model tests confirmed that our inversion method provided more accurate descriptions of wavefield propagation patterns within thin interbeds containing thin VTI beds using the Kennett's second-order approximations, compared to the method using the Zoeppritz equations. With < 30% random noise, the inversion results accurately matched the true model, indicating that this method exhibited strong noise resistance.

Compared to conventional methods, the proposed method requires more prior information and higher accuracy for the initial model, which must at least roughly reflect the variation trends of the subsurface physical parameters. Joint inversion was conducted in the PP time domain, necessitating the conversion of PS AVA gathers from the PS time domain to the PP time domain.

In the inversion of field data, we observed that the travel-time variations of internal multiples within thin interbeds were complex, and these multiples were coupled with primary reflections. Because the exact physical parameters of the media are often unavailable, accurately calculating the travel times of internal multiples becomes challenging, ultimately complicating the accurate time-domain conversion of internal multiples. Under the thin-layer and small-to-medium incidence angle assumptions, the time difference between the internal multiples and the primary reflections was relatively small. Therefore, we picked numerous horizons in the PP and PS AVA gathers to ensure that the primary reflections in the PS AVA gathers could be accurately compressed into the PP time domain. On this basis, we estimated the compression of the internal multiples in the PP domain. Moreover, we appropriately reduced the weight of the PS dataset in the inversion. Thus, this method compresses PS AVA gathers into the PP time domain with relatively high accuracy while minimizing the impact of time–domain conversion errors on inversion results.

When processing field data, the proposed method accounts for transmission losses and internal multiples, eliminating the need for transmission-loss compensation and multiple suppression, thereby distinguishing it from conventional preprocessing methods.

The proposed method is suitable for layers that can be considered VTI media. However, it is inapplicable to thin interbeds with internally dipping laminations, which exhibit azimuthal anisotropy effects and are better characterized as tilted transversely isotropic or horizontal transversely isotropic media. In addition, when inverting field data, the time-domain conversion for internal multiples employs an approximation method, potentially leading to errors in the inversion results. Finally, our method requires the construction of Thomsen anisotropy parameter models derived from P- and S-wave velocity logs. Therefore, if such velocity logs are unavailable in a study area, the proposed inversion method cannot be applied.

6. Conclusion

We propose a joint PP- and PS-wave AVA inversion method based on Kennett's second-order approximations for thin interbeds containing thin VTI beds. Our method considers thin beds with short-term cycle characteristics as thin VTI beds, using Kennett's second-order approximations to describe the wave propagation characteristics in thin interbeds containing thin VTI beds while considering internal multiples and transmission losses. The proposed method provides a more detailed characterization of the VTI properties of thin beds exhibiting short-term cycle characteristics within thin interbeds.

The inversion objective function for the five parameters is established based on the LM algorithm, which effectively controls model complexity via sparse constraints and enhances inversion stability and resilience to noise.

Synthetic model tests, conducted with and without noise, demonstrated the high precision and robustness of our inversion method in handling complex thin interbeds. The one- and two-dimensional inversion results of the multi-component field seismic data obtained using the proposed method align well with trends observed in well logs. This method enhances the inversion accuracy for thin interbeds and provides technical support for oil and gas exploration and for the geological interpretation of anisotropic thin interbeds.

Conflict of interest

Jun Lu serves as the Guest Editor of this Special Issue, but was not in any way involved in the editorial and peer-review process conducted for this paper, directly or indirectly. Other authors declare they have no competing interests.

Author contributions

Conceptualization: Jun Lu
Formal analysis: Peidong Huang, Jun Lu
Funding acquisition: Zhe Yang, Wei Yang
Investigation: Peidong Huang, Jun Lu, Chun Yang
Methodology: Peidong Huang, Jun Lu
Visualization: Peidong Huang
Writing–original draft: Peidong Huang
Writing–review & editing: Jun Lu, Chun Yang

Availability of data

Data are available upon request via lj615@cugb.edu.cn.

References

1. Buland A, Omre H. Bayesian linearized AVO inversion. *Geophysics*. 2003;68(1):185-198.

    doi: 10.1190/1.1543206

2. Huang G, Chen X, Luo C, Li X. Application of optimal transport to exact Zoeppritz equation AVA inversion. *IEEE Geosci Remote Sens Lett*. 2018;15(9):1337-1341.

    doi: 10.1109/lgrs.2018.2841916

3. Simmons JL, Backus MM. AVO modeling and the locally converted shear wave. *Geophysics*. 1994;59(8):1237-1248.

    doi: 10.1190/1.1443681

4. Fuchs K. The reflection of spherical waves from transition zones with arbitrary depth-dependent elastic moduli and density. *J Phys Earth*. 1968;16:27-41.

    doi: 10.4294/jpe1952.16.special_27

5. Fryer GJ. A slowness approach to the reflectivity method of seismogram synthesis. *Geophys J Int*. 1980;63(3):747-758.

    doi: 10.1111/j.1365-246X.1980.tb02649.x

6. Carcione JM. Amplitude variations with offset of pressure-seal reflections. *Geophysics*. 2001;66(1):283-293.

    doi: 10.1190/1.1444907

7. Carcione JM. Energy balance and fundamental relations in dynamic anisotropic poro-viscoelasticity. *Proc R Soc Lond A*. 2001;457:331-348.

    doi: 10.1098/rspa.2000.0669

8. Liu H, Li J, Chen X, Hou B, Chen L. Amplitude variation with offset inversion using the reflectivity method. *Geophysics*. 2016;81(4):R185-R195.

    doi: 10.1190/geo2015-0332.1

9. Kennett BLM. *Seismic Wave Propagation in Stratified Media*. Cambridge, UK: Cambridge University Press; 1983.

10. Rubino JG, Velis D. Thin-bed prestack spectral inversion. *Geophysics*. 2009;74(4):R49-R57.

    doi: 10.1190/1.3148002

11. Padhi A, Mallick S. Multicomponent pre-stack seismic waveform inversion in transversely isotropic media using a non-dominated sorting genetic algorithm. *Geophys J Int*. 2014;196(3):1600-1618.

    doi: 10.1093/gji/ggt460

12. Lu Y, Peng S, Cui X, Li D, Wang K. Thin-Bed Inversion using Pre-Stack Seismic Data. In: *SEG International Exposition and Annual Meeting*, San Antonio, TX, USA; 2019.

    doi: 10.1190/segam2019-3214870.1

13. Yang Z, Lu J. Second-order approximation of the seismic reflection coefficient in thin interbeds. *Energies*. 2020;13(6):1465.

14. Yang C, Wang Y. Joint PP-PS seismic prestack inversion of thin-bed reservoirs. *J Geophys Eng*.2022; 19(4):897-913.

    doi: 10.1093/jge/gxac060

15. Kuai Z, Cao D, Jin C. Frequency-Dependent Reflection Characteristics of Single Thin Layer and Waveform Inversion. In: *SEG/AAPG International Meeting for Applied Geoscience and Energy*, Houston, TX, USA; 2023.

    doi: 10.1190/image2023-3916363.1

16. Chen J, Glinsky ME. Stochastic inversion of seismic PP and PS data for reservoir parameter estimation. *Geophysics*. 2014;79(6):R233-R246.

    doi: 10.1190/geo2013-0456.1

17. Wang D, Zhang M, Wang J, Chen D, Zhao Y, Bai J. Research and application of joint interpretation using P-wave and PS-wave in tight gas exploration. *J Earth Sci*. 2024;35(4):1402-1406.

    doi: 10.1007/s12583-024-1995-7

18. Veire HH, Landrø M. Simultaneous inversion of PP and PS seismic data. *Geophysics*. 2006;71(3):R1-R10.

    doi: 10.1190/1.2194533

19. Lu J, Wang Y, Chen J, An Y. Joint anisotropic amplitude variation with offset inversion of PP and PS seismic data. *Geophysics*. 2018;83(2):N31-N50.

    doi: 10.1190/geo2016-0516.1

20. Rüger A. *Reflection Coefficients and Azimuthal AVO Analysis in Anisotropic Media*. Tulsa, OK, USA: Society of Exploration Geophysicists; 2002.

    doi: 10.1190/1.9781560801764

21. Luo C, Ba J, Carcione JM, Huang G, Guo Q. Joint PP and PS pre-stack seismic inversion for stratified models based on the propagator matrix forward engine. *Surv Geophys*. 2020;41(5):987-1028.

    doi: 10.1007/s10712-020-09605-5

22. Tura A, Simmons J, Daneshvar S, Copley M, Stitt, J. Improving reservoir characterization and time-lapse seismic through joint inversion of PP- and PS-wave seismic data. *Interpretation*. 2022;10(2):T341-T350.

    doi: 10.1190/int-2021-0167.1

23. Yang Y, Yin X, Li K. Quadratic reflectivity-based joint PP and PS inversion for VTI media using the stiffness matrix. *IEEE Trans Geosci Remote Sens*. 2024;62:1-13.

    doi: 10.1109/tgrs.2024.3492394

24. Huang PD, Lu J, Wang Y. Second-order approximate reflection coefficients of vertical transversely isotropic thin beds. *Acta Geophys*. 2022;70(3):1155-1169.

doi: 10.1007/s11600-022-00758-y

25. Levenberg K. A method for the solution of certain non-linear problems in least squares. *Quarterly Appl Math*. 1944;2(2):164-168.

    doi: 10.1090/qam/10666

26. Marquardt DW. An algorithm for least-squares estimation of nonlinear parameters. *J Soc Ind Appl Math*. 1963;11(2):431-441.

    doi: 10.1137/0111030

27. Graebner M. Plane-wave reflection and transmission coefficients for a transversely isotropic solid. *Geophysics*. 1992;57(11):1512-1519.

    doi: 10.1190/1.1443219

28. Thomsen L. Weak elastic anisotropy. *Geophysics*. 1986;51(10):1954-1966.

    doi: 10.1190/1.1442051

29. Backus GE. Long-wave elastic anisotropy produced by horizontal layering. *J Geophys Res*. 1962;67(11):4427-4440.

    doi: 10.1029/jz067i011p04427